2.26
Magnetic Circular Dichroism of Paramagnetic Species

E. I. SOLOMON, M. L. NEIDIG, and G. SCHENK
Stanford University, Stanford, CA, USA

2.26.1 INTRODUCTION

Magnetic circular dichroism (MCD) spectroscopy and variable-temperature variable-field (VTVH) MCD are powerful methods for studying the excited and ground states of paramagnetic systems. Notably, these methods provide detailed insight into the geometric and electronic structures of catalytically active centers in inorganic and biological systems. In this review, we present the theoretical background for MCD and VTVH MCD and discuss their application.

2.26.2 BASIC PRINCIPLES AND APPLICATIONS OF MCD AND VTVH MCD

2.26.2.1 MCD

MCD spectroscopy combines the CD experiment with a longitudinal magnetic field, where the application of the magnetic field induces optical activity in any material so that all substances exhibit MCD activity. MCD probes the Zeeman splittings in the ground and excited states and the field-induced mixing between states.

MCD intensity for a transition from a ground state $|A\rangle$ to an excited state $|J\rangle$ is given by Equation (1):

$$\frac{\Delta A}{E} = \left(\frac{2N_0\pi^3\alpha^2 Cllge}{250\,hcn}\right)\beta H\left[\boldsymbol{A}_1\left(\frac{-\delta f(E)}{\delta E}\right) + \left(\boldsymbol{B}_0 + \frac{\boldsymbol{C}_0}{kT}\right)f(E)\right] \quad (1)$$

for broadband transitions when the MCD intensity is linear with field. Here, ΔA is the field-dependent difference between left- and right-circularly polarized light (lcp and rcp, respectively) absorption, $E = h\nu$, α is the electric permeability, $\boldsymbol{C}$ is the concentration, l is the path length, n is

the index of refraction, β is the Bohr magneton, H is the applied magnetic field, $f(E)$ is the absorption bandshape and $\delta f(E)/\delta(E)$ is its first derivative.[1–5] $\boldsymbol{A}_1$, $\boldsymbol{B}_0$, and $\boldsymbol{C}_0$ are the MCD ***A***-, ***B***-, and ***C***-terms, respectively. Note from Equation (1) that MCD intensity increases linearly with increasing magnetic field, while only C-term intensity is inversely proportional to temperature in the linear limit where $kT \gg g\beta H$.

2.26.2.1.1 A-, B-, and C-terms

$\boldsymbol{A}_1$ and $\boldsymbol{C}_0$ (see Chapter 2.14 for further details) are related to molecular electronic structure by Equations (2) and (3), where $|J\rangle$ is the excited state of the corresponding MCD transition, $|d_A|$ is the electronic degeneracy of the ground state $|A\rangle$ and the summation is over all components of $|A\rangle$ and $|J\rangle$. The first part of the ***A***-term expression is the difference between the excited and ground-state Zeeman terms, while the first part of the ***C***-term expression gives the Zeeman effect in the ground state. The second parts in both equations give the difference between the lcp (m_+) and rcp (m_-) electric dipole moments:

$$\boldsymbol{A}_1 = \frac{1}{|d_A|}\sum(\langle J|L_z + 2S_z|J\rangle - \langle A|L_z + 2S_z|A\rangle) \times (|\langle A|m_-|J\rangle|^2 - |\langle A|m_+|J\rangle|^2) \tag{2}$$

$$\boldsymbol{C}_0 = \frac{-1}{|d_A|}\sum\langle A|L_z + 2S_z|A\rangle(|\langle A|m_-|J\rangle|^2 - |\langle A|m_+|J\rangle|^2) \tag{3}$$

From the electric dipole term in Equations (2) and (3), the MCD selection rule is $\Delta M_L = \pm 1$, requiring that either the ground or excited state contains orbital angular momentum. Therefore, ***A***- and ***C***-term MCD transitions observed between spin degenerate orbital singlets occur by spin–orbit mixing with other states.

From Equation (2), either a degenerate ground or excited state is required for a system to exhibit ***A***-term intensity, whereas from Equation (3) ***C***-terms require a degenerate ground state. Figure 1 illustrates the ***A***- and ***C***-term mechanisms for a molecule having an angular momentum of $J = 1/2$ in the ground and excited states. In the absence of a magnetic field, the rcp and lcp transitions from the doubly degenerate ground state to the doubly degenerate excited state cancel, resulting in no observed MCD intensity. At high temperatures ($kT \gg g\beta H$) in the presence of a magnetic field (Figure 1a), the degeneracies of the ground and excited states are removed so that the rcp and lcp transitions combine to give an MCD transition with a derivative shape (temperature-independent ***A***-term). At lower temperatures ($kT \sim g\beta H$, Figure 1b), the lowest energy sublevel of the ground state is more populated than the higher energy sublevel, resulting in an intense ***C***-term MCD transition with an absorption bandshape:

$$\boldsymbol{B}_0 = \frac{2}{|d_A|}\mathrm{Re}\sum\left[\begin{array}{l}\displaystyle\sum_{K(K\neq J)}\frac{\langle J|L_z+2S_z|K\rangle}{\Delta E_{KJ}}(\langle A|m_-|J\rangle\langle K|m_+|A\rangle - \langle A|m_+|J\rangle\langle K|m_-|A\rangle) \\ \displaystyle + \sum_{K(K\neq A)}\frac{\langle K|L_z+2S_z|A\rangle}{\Delta E_{KA}}\big(\langle A|m_-|J\rangle\langle J|m_+|K\rangle - \langle A|m_+|J\rangle\langle J|m_-|K\rangle\big)\end{array}\right] \tag{4}$$

The relation between the $\boldsymbol{B}_0$-term and molecular properties is given by Equation (4), and is described in more detail in Chapter 2.14. ***B***-term intensity arises from field-induced mixing between the ground state $|A\rangle$ or excited state $|J\rangle$ and an intermediate state, $|K\rangle$, which is required to be close in energy. The first summation on the right of Equation (4) gives the Zeeman mixing of the intermediate state $|K\rangle$ into the excited state $|J\rangle$, and the second summation gives the Zeeman mixing of $|K\rangle$ into the ground state $|A\rangle$. From Equation (1) ***B***-term signals are temperature independent and have an absorption shape.

2.26.2.1.2 C-terms and paramagnetic systems

Though all three mechanisms (***A***-, ***B***-, and ***C***-term) may contribute to the MCD intensity for a paramagnetic species, the ***C***-term dominates at low temperature (see Equation (1)). As ground

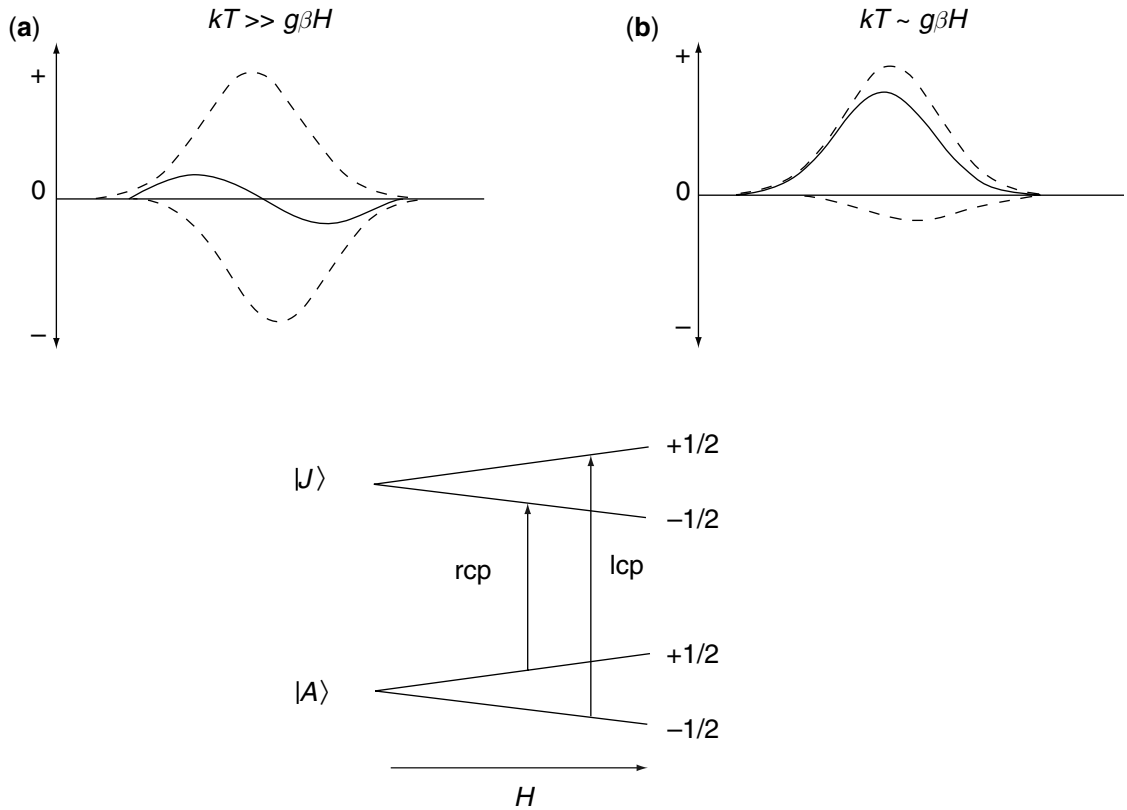

Figure 1 MCD mechanism for a molecule with $J = 1/2$ in the ground and excited states. (a) derivative shaped ***A***-term and its components when $kT \gg g\beta H$ and (b) absorption shaped ***C***-term and its component when $kT \sim g\beta H$. The selection rules for transitions of rcp and lcp light between the degenerate ground and excited states split by a magnetic field is shown at the bottom.

states are generally orbitally nondegenerate, the ground state degeneracy required for ***C***-term intensity usually involves the spin. From the selection rules for the MCD transition ($\Delta M_L = \pm 1$, $\Delta M_S = 0$), a nonzero ***C***-term is only obtainable from spin degeneracy through spin–orbit coupling (SOC). For high-symmetry paramagnetic metal species, orbitally doubly degenerate excited states exist having orbital angular momentum which will spin–orbit couple to the electron spin and produce a splitting of the excited state. A temperature-dependent pseudo-***A***-term will be produced from equal and opposite ***C***-terms, with the energy splitting of the ***C***-terms giving the in-state SOC. Pseudo-***A***-terms quantify the excited state SOC, allow assignment of orbitally degenerate excited states and have a sign, which can provide further insight into the one-electron orbitals involved in the transition.[6]

Most paramagnetic metal sites in biological systems have low symmetry and no orbital degeneracy. Thus, the ground-to-excited-state transition is electric-dipole allowed, but with a unidirectional transition moment in the molecule. From the expression for $\boldsymbol{C}_0$ for a frozen solution averaged over all molecular orientations relative to the external magnetic field in Equation (5), the selection rule for MCD intensity requires two perpendicular nonzero transition moments.[7] This condition is met for low-symmetry species with orbitally nondegenerate states through SOC, whereby two excited states with transition moments in different directions are mixed, resulting in nonzero ***C***-term intensity.[8] The coupling between two excited states will produce equal and opposite ***C***-terms, yielding a pseudo-***A***-term derived from nondegenerate states. More generally, SOC among a complete set of excited states should result in equal and opposite ***C***-term intensity distributed over the states, which will sum to zero. Any net ***C***-term intensity summed over excited states will result from further SOC into the ground state:

$$\boldsymbol{C}_0 \propto g_z M_x M_y + g_y M_x M_z + g_x M_y M_z \tag{5}$$

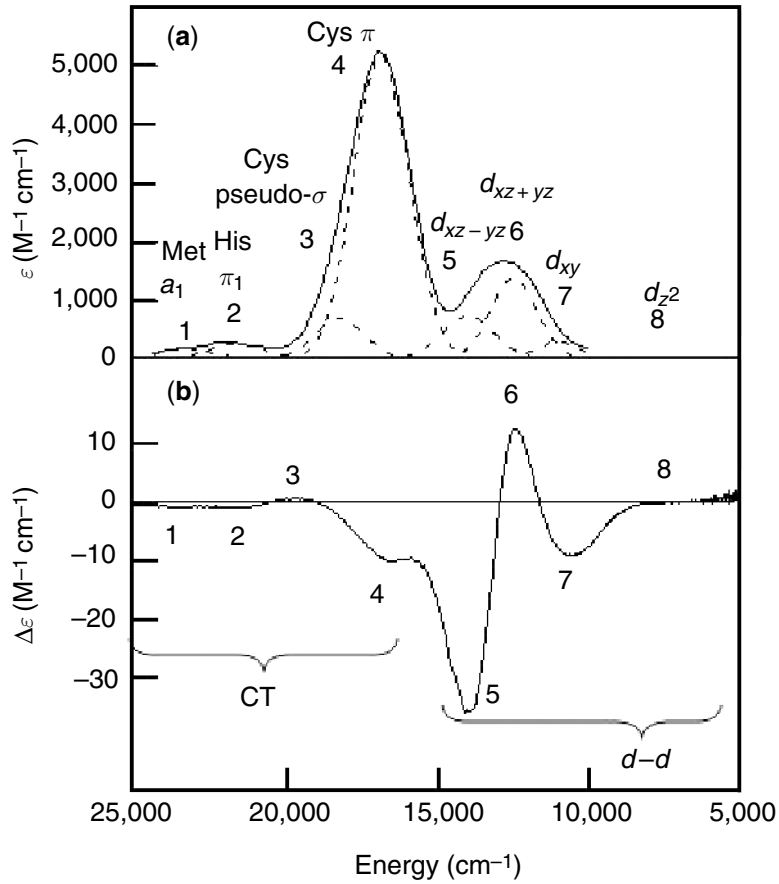

Figure 2 Low-temperature (a) absorption and (b) MCD of the blue copper protein plastocyanin. The use of $\boldsymbol{C}_0/\boldsymbol{D}_0$ led to the assignment of bands 1–4 to CT transitions and bands 5–8 to $d \rightarrow d$ transitions.

Thus, SOC determines the $\boldsymbol{C}$-term intensity, which is dependent on the magnitude of the SOC constant. Since the SOC constant will be greater for metal-centered than ligand-centered transitions, $d \rightarrow d$ excited states are expected to be more spin–orbit mixed than ligand-based charge transfer (CT) states and show larger low-temperature MCD intensity relative to absorption intensity. The MCD-to-absorption intensity ratio is often expressed as $\boldsymbol{C}_0/\boldsymbol{D}_0$, which is given experimentally by Equation (6):

$$\frac{\boldsymbol{C}_0}{\boldsymbol{D}_0} = \frac{kT}{\beta H}\left(\frac{\Delta\varepsilon}{\varepsilon}\right) \tag{6}$$

The application of low-temperature MCD and $\boldsymbol{C}_0/\boldsymbol{D}_0$ analyses to paramagnetic metal sites in biological systems has been a powerful method for identifying and studying $d \rightarrow d$ transitions. In addition, the sign and magnitude of the $\boldsymbol{C}_0/\boldsymbol{D}_0$ value allows the rigorous assignment of bands based upon electronic structure calculations, which include SOC and, thus, probe specific bonding interactions. Figure 2 shows the low-temperature MCD spectrum of the blue copper protein plastocyanin, where this method has been successfully applied to assign bands 5–8 to $d \rightarrow d$ transitions as these transitions are weak in absorption but intense in low-temperature MCD (bands 1–4 are assigned to CT transitions).[9] The assignments of these bands are given by the signs of the $\boldsymbol{C}$-terms and, thus, rigourously determined by the MCD experiment. These $d \rightarrow d$ transitions could then be used to correlate to crystallographically determined geometric structures and generate an electronic structure description of the plastocyanin active site.

2.26.2.2 VTVH MCD

Historically, MCD has mainly been used to probe the excited states of paramagnetic systems. More recently, this methodology has gained significance since it also provides insight into ground state

properties,[10] for example in ferrous systems, which are often inaccessible to EPR spectroscopy.[11] In the previous section the terms contributing to an MCD transition have been discussed. In particular, the ***C***-term contribution is greatly enhanced at low temperatures and high fields (see Equation (1)). In Figure 3 the dependence of the MCD intensity on the magnetic field at a fixed temperature is illustrated for a system with $S = 1/2$. At sufficiently low field the intensity increases linearly; at higher fields the intensity starts to level off and then saturates. The origin of this saturation behavior is developed from the insert in Figure 3a. In the absence of a magnetic field the $M_S = |1/2\rangle$ and $|-1/2\rangle$ sublevels of both states are degenerate and the right and left circularly polarized transitions cancel. Application of a field removes this degeneracy; the sublevels are split by the Zeeman term ($g\beta H$). As the field is increased and the temperature lowered, the $|-1/2\rangle$ sublevel of the ground state is dominantly Boltzmann populated, until, at low temperatures and high fields only this level is significantly populated. In this example only the lcp transition is observed and, thus, the MCD

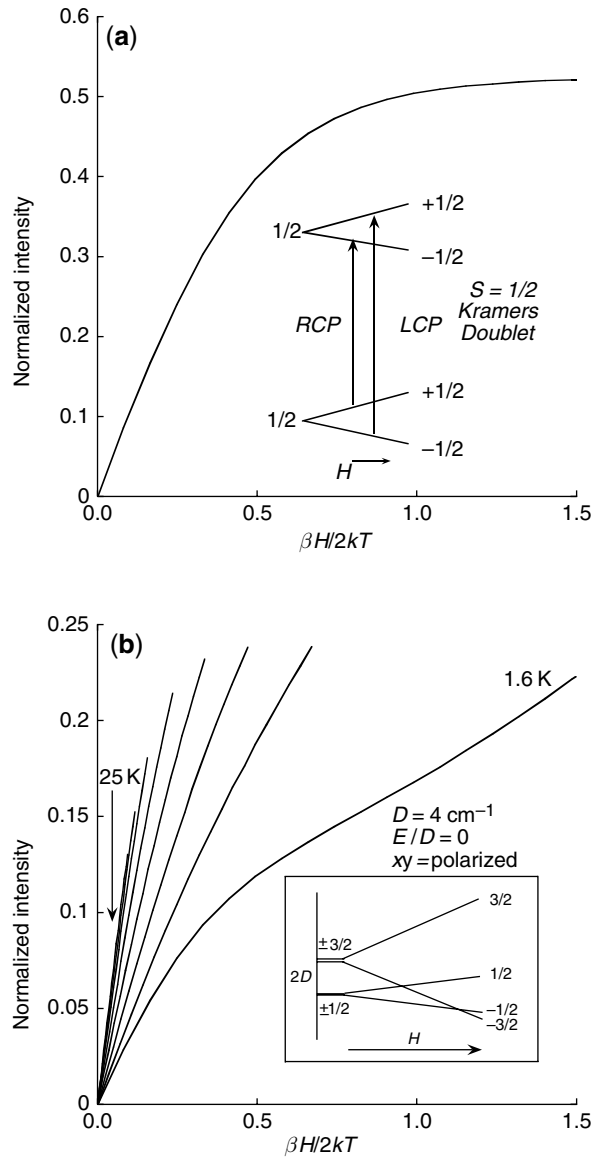

Figure 3 Field dependence of the MCD signal. (a) Saturation magnetization MCD for an $S = 1/2$ Kramers doublet. The inset shows a schematic representation of the transitions for lcp and rcp light from the ground to the excited state. (b) Simulation of the VTVH MCD behavior of an xy polarized transition for an axial $S = 3/2$ system with positive ZFS ($D = 4\,\mathrm{cm}^{-1}$, $E/D = 0$). The inset shows the energy splitting of the M_S sublevels as a function of the magnetic field, aligned along the z-axis.

signal saturates. The dependence of the intensity on the field is described by the Brillouin-type function for an isotropic $S = 1/2$ system:

$$\Delta\varepsilon = \text{const} \tanh\left(\frac{g\beta\mathrm{H}}{2kT}\right) \tag{7}$$

For a system with octahedral or tetrahedral symmetry, saturation data collected at different temperatures superimpose for all spin systems. For low-symmetry sites (e.g., protein-active sites) only isotherms for $S = 1/2$ systems superimpose in general. The spread or nesting behavior observed in VTVH MCD for systems with $S \neq 1/2$ is ascribed to the zero-field splitting (ZFS) of the M_S sublevels of the ground state, and is discussed in the next sections, first for Kramers-type systems (half-integer spin) and then for non-Kramers ions (integer spin), as exemplified by Fe^{II}.

2.26.2.2.1 Kramers ions

The VTVH MCD behavior for systems with $S > 1/2$ is complicated by the fact that the ground state is not a single doublet as in an $S = 1/2$ system. For illustrative purposes the case of an $S = 3/2$ system is discussed. Kramers theorem[12] postulates that for a system with half-integer spin all energy levels must be at least twofold degenerate. Application of a magnetic field removes the remaining degeneracies, as shown in Figure 3b for an $S = 3/2$ with positive ZFS (*vide infra*), removing the fourfold spin degeneracy of the quartet ground state, resulting in two doubly degenerate levels with $M_S = \pm 1/2$ and $M_S = \pm 3/2$ (Figure 3b inset). The energy levels are described by an effective spin Hamiltonian including the Zeeman effect and the ZFS. Assuming the D-tensor and the *g*-matrix to be coaxial, the energy levels are calculated using Equation (8):[13]

$$\mathcal{H}_{\text{spin}} = D[S_z^2 - 5/4] + E[S_x^2 - S_y^2] + \beta(g_x H_x S_x + g_y H_y S_y + g_z H_z S_z) \tag{8}$$

Here, D and E are the axial and rhombic ZFS parameters, respectively. Application of Equation (8) to the spin functions $|S, M_S\rangle$ with $S = 3/2$ results in a fourth order equation, which describes the behavior of the four energy levels in Figure 3b as a function of the magnitude of the external field and its orientation relative to the molecular frame. For an exact solution for the spin Hamiltonian the 4×4 matrix must be diagonalized at every field. For Kramer ions the parameters D and E can generally be determined by EPR spectroscopy.

VTVH MCD data for systems with $S > 1/2$ are in general more difficult to analyze than $S = 1/2$ systems, but additional information may be gained about the paramagnetic site.[11,14] Importantly, from the MCD magnetization curves the polarizations for each transition can be obtained, even for randomly oriented frozen samples.[14–16] Since MCD spectroscopy is orientation selective, only molecules that are suitably aligned in the magnetic field contribute to MCD intensity. For large ZFS, the $S = 3/2$ system can be approximated as a collection of non-interacting doublets. However, if the magnitude of D is similar to the Zeeman term ($g\beta H$), crossing between the spin levels has to be taken into account. A general expression (Equation (9)) for the analysis of VTVH MCD saturation magnetization curves[14] was derived, where the summation is carried out over all levels i of the ground state:

$$\frac{\Delta\varepsilon}{E} = \frac{\text{const}}{4\pi S}\int_0^{\pi}\int_0^{2\pi}\sum_i N_i(l_x\langle S_x\rangle_i M_{yz}^{\text{eff}} + l_y\langle S_y\rangle_i M_{xz}^{\text{eff}} + l_z\langle S_z\rangle_i M_{xy}^{\text{eff}})\sin\theta\,\mathrm{d}\theta\,\mathrm{d}\phi \tag{9}$$

which reduces to

$$\frac{\Delta\varepsilon}{\mathrm{E}} = -\frac{\text{const}}{4\pi}\int_0^{\pi}\int_0^{2\pi}\tanh\left(\frac{\gamma\beta\mathrm{H}}{2k\mathrm{T}}\right)\frac{\sin\theta}{\gamma}(l_x^2 g_x M_{yz}^{\text{eff}} + l_y^2 g_y M_{xz}^{\text{eff}} + l_z^2 g_z M_{xy}^{\text{eff}})\,\mathrm{d}\theta\,\mathrm{d}\phi \tag{10}$$

where $\gamma = \sqrt{G_x^2 + G_y^2 + G_z^2}$ and $G_p = l_p g_p$ with $p = x,y,z$ for a system with $S = 1/2$. E is the photon energy, N_i is the Boltzmann population of the i-th sublevel, $\langle S_p\rangle$ are the spin expectation

values in the p direction ($p = x, y, z$), l_p are the direction cosines describing the orientation of the applied field with respect to the molecular coordinate system, g_p are g-values of the molecule and M_{ij}^{eff} are the products of the relative polarizations of two electronic transitions. The angles between the incident light and the molecular z-axis and the xy plane are described by θ and Φ, respectively. These equations are valid for any system with an orbitally non-degenerate ground state with $S \geq 1/2$; note that for an isotropic system Equation (10) simplifies to a Brillouin-type function shown in Equation (7). In Figure 3b a simulation of the VTVH MCD behavior of an $S = 3/2$ system is shown, with $D = +4\,\text{cm}^{-1}$, $E/D = 0$ and the transition is assumed to be xy polarized. The saturation curves can readily be understood by an inspection of Equation (9). Since the transition is xy polarized only the third term contributes to MCD intensity, which selects the molecules whose z-axes are aligned along the magnetic field (g_z). At lowest temperature and low fields the $M_S = -1/2$ is lowest in energy (Figure 3b). Increasing the field gradually increases the Boltzmann population of this level, until at $\beta H/2kT = \sim 0.4$ the intensity starts to level off. However, no saturation of the signal is observed. This is due to the crossing between the $M_S = -1/2$ and $M_S = -3/2$ levels (Figure 3b). Since the spin expectation value for the latter is larger ($\langle S_z \rangle = 3/2$ compared to 1/2 for the former) the intensity increases. At higher temperatures the inflection point is less apparent since the $M_S = \pm 3/2$ doublet is thermally populated.

In principal, Equation (9) can be applied to obtain ground state parameters (g-values and ZFS parameters D and E) and the products of the relative polarizations. However, for VTVH MCD fitting the most reliable method is to determine the g-values and ZFS parameters from temperature-dependent EPR spectroscopy (Equation (8)) and calculate the effective polarization products with Equation (9) since this procedure reduces the number of variables in the fitting routine. From the M_{ij}^{eff} obtained, the polarizations in the p direction ($p = x, y, z$) can be determined using the following expression:

$$\%x = 100 \times \frac{(M_{xy}^{\text{eff}} M_{xz}^{\text{eff}})^2}{(M_{xy}^{\text{eff}} M_{xz}^{\text{eff}})^2 + (M_{xy}^{\text{eff}} M_{yz}^{\text{eff}})^2 + (M_{xz}^{\text{eff}} M_{yz}^{\text{eff}})^2} \tag{11}$$

where cyclic permutations of the p indices provide the other polarizations. Transitions polarized along different directions show a distinct nesting behavior that enables the determination of the polarization of a band in a spectrum and can be used to assign transitions. Test calculations show that the VTVH MCD behavior is (i) a weak function of E/D, (ii) a strong function of the sign of the ZFS parameter D, (iii) moderately sensitive towards the absolute magnitude of D, and (iv) strongly dependent on both the sign and magnitude of the polarization products M_{ij}^{eff}.

An example of an $S = 3/2$ system is the NO derivative of the mononuclear non-heme iron enzyme protocatechauate 3,4-dioxygenase (PCD), a member of the intradiol dioxygenases.[17] PCD catalyzes the cleavage of protocatechuate (PCA) to β-carboxy-*cis,cis*-muconate, with the incorporation of both atoms from molecular oxygen. Although an oxygen intermediate has been observed by stopped-flow spectroscopy[18] it cannot be trapped in sufficient amounts for spectroscopic analysis. In a recent study, NO was used as an O_2 analog to study the electronic structure of potential reaction intermediates.[19] NO reacts with the ferrous form of PCD to form an antiferromagnetically coupled Fe^{III}–NO^- complex. For the substrate-bound form the ZFS parameters D and E/D were estimated to be $4\,\text{cm}^{-1}$ and 0.175, respectively, using EPR spectroscopy.[20] The MCD spectrum and VTVH MCD saturation curves for five bands are shown in Figure 4; the effective polarization products M_{ij}^{eff} and the relative polarizations as determined with Equation (11) are summarized in Table 1. Often, NO reacts with Fe^{II} to form a short, strong bond with an Fe—N distance of around 1.75 Å (e.g., ref. 21). However, in the case of substrate-bound PCD the intermediate rhombicity observed from EPR indicates the absence of a dominating strong direction within the complex. This is in agreement with XAS pre-edge and EXAFS measurements, which preclude the presence of a single strong direction. VTVH MCD indicates that both bands 1 and 4 in Figure 4, assigned as a substrate to Fe^{III} CT transitions[19], define the dominant (z) direction. The remaining bands 2, 3, and 5 are x-polarized (Table 1), but attributed to the NO^- ligand from previous studies on Fe–NO model complexes.[21] Band 2 contains two weak, formally forbidden $Fe^{III} d \rightarrow d$ transitions, band 3 the two in-plane NO^- $2\pi^*$ to d_{xz} and $d_{x^2-y^2}$ CT transitions, and band 5 the intense out-of-plane NO^- $2\pi^*$ to d_{yz} CT transition. Hence, VTVH MCD provides direct insight into the electronic and geometric structure of the substrate- and NO-bound active site of PCD, revealing that, in contrast to most known high-spin Fe^{III}–NO^- complexes, the substrate and not the NO ligand defines the strongest bond due to the strong donor interaction from this catecholate ligand.

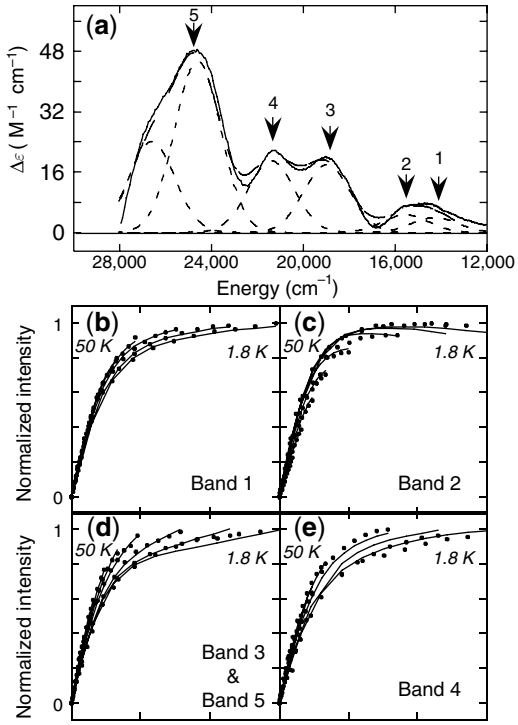

Figure 4 (a) Gaussian resolution (---) of the MCD spectrum of PCA- and NO-bound PCD at 5 K and 7 T. VTVH MCD data at various temperatures (ranging from 1.6 K to 50 K) and magnetic fields (between 0 T and 7 T) were collected at positions indicated by arrows: Band 1 (b) at 14,100 cm^{-1}, Band 2 (c) at 15,500 cm^{-1}, Band 3 (d) at 19,100 cm^{-1}, Band 4 (e) at 21,300 cm^{-1}, and Band 5 (d) at 24,780 cm^{-1}. Note that identical saturation behavior was observed for Bands 3 and 5, indicating that they have the same polarization.

Table 1 Effective transition moments from the VTVH MCD data for substrate- and NO-bound PCD.[19]

Transition	M_{xy}	M_{xz}	M_{yz}	*Polarization*
Band 1	0.22	1.1	0.5	z
Band 2	−1.0	1.7	0.28	x
Band 3 + 5	2.1	1.2	−0.50	x
Band 4	0.11	0.76	1.0	z

This observation is of functional significance since it supports a mechanism where the reduction potential of the iron is sufficiently lowered to favor substrate activation by Fe^{III}.[19]

2.26.2.2.2 Non-Kramers ions

The analysis of VTVH MCD data from non-Kramers-type systems has been reviewed previously [8,11,22,23] and is illustrated in brief for a ferrous system ($S = 2$) with negative ZFS (Figure 5, right panel). The VTVH MCD behavior of $S = 2$ systems with positive ZFS qualitatively resembles negative ZFS systems with a large δ and is thus not further discussed here.[11] Note, however, that the sign of ZFS relates to the geometry of the active site; negative and positive signs correspond to a weak and strong tetragonal distortion, respectively. For an $S = 2$ system with negative ZFS the $M_S = \pm 2$ doublet is lowest in energy (Figure 5). In contrast to Kramers-type systems a rhombic distortion splits this doublet (by an amount characterized by δ (Figure 5)) even in the absence of an external magnetic field. This splitting of the $M_S = \pm 2$ sublevel is the origin of the nesting which is generally observed for the saturation magnetization MCD data for non-Kramers ions as illustrated in Figure 6a. When these data are replotted to separate temperature from field dependence (Figure 6b), it is observed that at low-temperature saturation the MCD intensity

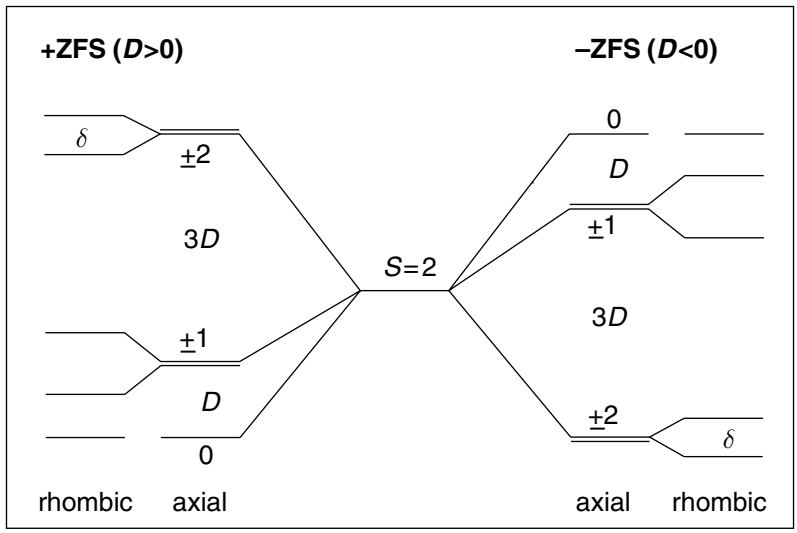

Figure 5 Energy splittings of the $S = 2$ sublevels for + ZFS (left) and –ZFS (right). In contrast to Kramers-type systems, rhombic distortion removes the degeneracy of the $M_S \geq \pm 1$ levels even in the absence of an external magnetic field.

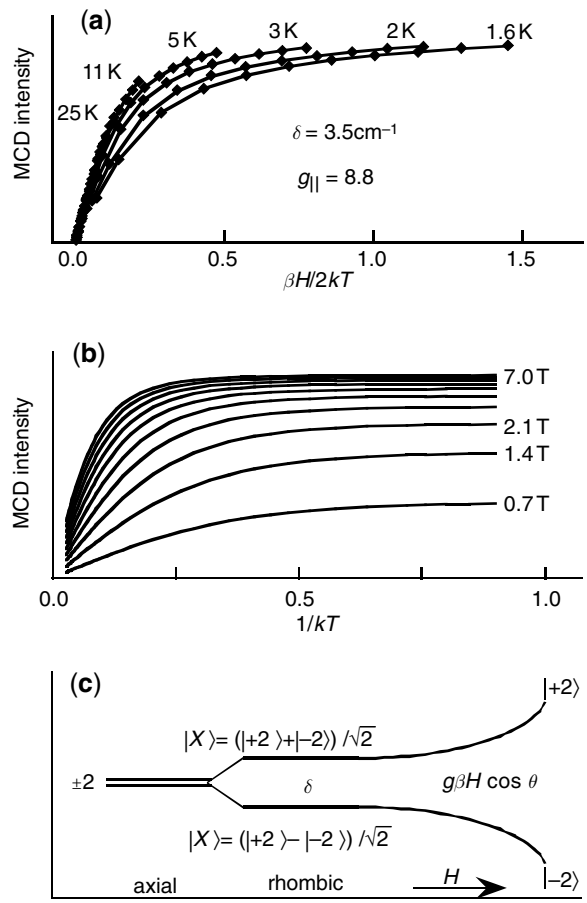

Figure 6 VTVH MCD data for a non-Kramers $S = 2$ system with negative ZFS (a). Replot of the data in Figure 6a to separate the temperature and field dependence. Note the increase in MCD intensity at low temperature saturates with increasing magnetic field (b). Rhombic and magnetic field splitting and mixing of an $M_S = \pm 2$ non-Kramers doublet (c).

increases in a nonlinear fashion, converging at high fields. This indicates that the wave function of the lowest component of the ground state is changing as a function of the magnetic field. This behavior is anticipated for a non-Kramers system, where rhombic distortion leads to a splitting of the $MS = \pm 2$ doublet (Figure 5). In the absence of a magnetic field the distortion leads to a mixing of the wave functions to produce $|X\rangle = (|+2\rangle + |-2\rangle)/\sqrt{2}$ and $|Y\rangle = (|+2\rangle - |-2\rangle)/\sqrt{2}$; equal amounts of $|+2\rangle$ and $|-2\rangle$ are mixed resulting in zero MCD intensity. As the field is increased the $MS = \pm 2$ doublet is further split by the amount $g\beta H\cos\theta$ (Figure 6c) and unequal amounts of $|+2\rangle$ and $|-2\rangle$ are mixed in a nonlinear fashion into the wave functions $|X\rangle$ and $|Y\rangle$ until they approach pure $|+2\rangle$ and $|-2\rangle$ at high magnetic field. It is this field dependence of the ground state wave function which leads to the observed saturation magnetization behavior in Figure 6a. In principal, the expression in Equation (9) can be applied to analyze VTVH MCD data, since this equation does not impose any restrictions on the spin of the system.[14] An expression that includes the non-Kramers behavior decribed above for a system with negative ZFS, and where the wave function is field-dependent, is given in Equation (12) (including orientation averaging)[11]

$$\Delta\varepsilon = \text{const}\left\{\int_0^{\pi/2} \frac{\cos^2\theta\,\sin\theta}{\Gamma} g_{\|}\beta H \tanh\left(\frac{\Gamma}{2kT}\right)\mathrm{d}\theta - \sqrt{2}\left(\frac{M_z}{M_{xy}}\right)\int_0^{\pi/2} \frac{\sin^3\theta}{\Gamma} g_{\perp}\beta H \tanh\left(\frac{\Gamma}{2kT}\right)\mathrm{d}\theta\right\} + B_0 H \quad (12)$$

where $= \sqrt{\delta^2 + (g_{\|}\beta H\cos\theta)^2 + (g_{\perp}\beta H\sin\theta)^2}$

which simplifies to Equation (7) for a simple isotropic system with $S = 1/2$, and includes a linear B-term to account for additional interactions amongst levels. VTVH MCD data can be computationally fit to Equation (12) to extract the ZFS splitting of the non-Kramers doublet ground state (δ), the ground state g-values ($g_{\|}$ and $g_{\perp}$), as well as the polarization ratio M_z/M_{xy}. Thus, VTVH MCD measurements on a non-Kramers system allow the determination of EPR parameters for a ground state that is often not accessible by EPR. For Fe^{II}-active sites these ground state parameters can be directly related to the ligand field parameters Δ and V (Scheme 1), which describe the splitting of the $^5T_{2g}$ ground state.[11] This provides a description of the t_{2g} d-orbital energies and a probe of specific metal–ligand π-interactions. In conclusion, the combination of these t_{2g} d-orbital splittings plus the e_g splittings observed by MCD (see ref. 11 for details) gives a complete energy-level diagram of the five d-orbitals of a metal ion site, and hence provides an experimental probe of its geometric and electronic structure.

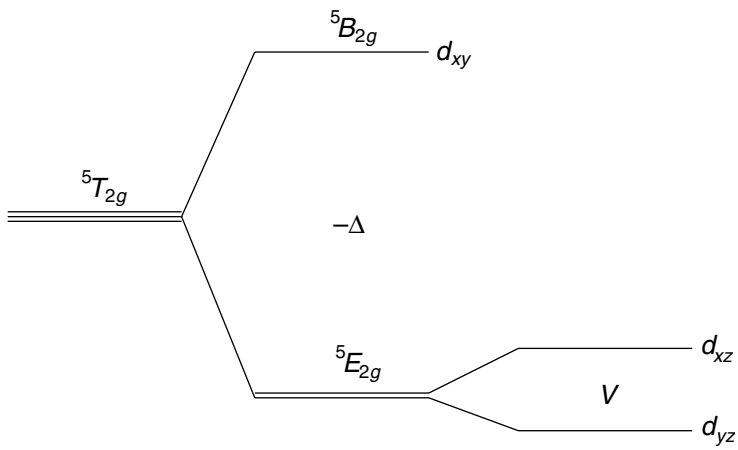

Scheme 1

ACKNOWLEDGMENTS

This work was supported by the National Institutes of Health (GM-40392 to E.I.S.).

2.26.3 REFERENCES

1. Buckingham, A. D.; Stephens, P. J. *Annu. Rev. Phys. Chem.* **1966**, *17*, 399–419.
2. Stephens, P. J. *J. Chem. Phys.* **1970**, *52*, 3489–3516.
3. Stephens, P. J. *Annu. Rev. Phys. Chem.* **1974**, *25*, 201–232.
4. Stephens, P. J. *Adv. Chem. Phys.* **1976**, *35*, 197–264.
5. Piepho, S. B.; Schatz, P. N. *Group Theory in Spectroscopy: With Application to Magnetic Circular Dichroism*; John Wiley: New York, 1983.
6. Gebhard, M. S.; Deaton, J. C.; Koch, S. A.; Millar, M.; Solomon, E. I. *J. Am. Chem. Soc.* **1990**, *112*, 2217–2231.
7. Thomson, A. J.; Cheesman, M. R.; George, S. J. *Methods Enzymol.* **1993**, *226*, 199–232.
8. Solomon, E. I.; Hanson, M. A. *Bioinorganic Spectroscopy*. In Inorganic Electronic Structure and Spectroscopy; Solomon, E. I., Lever, A. B. P., Eds.; Wiley: New York, 1999; Vol. 2, pp 1–129.
9. Gewirth, A. A.; Solomon, E. I. *J. Am. Chem. Soc.* **1988**, *110*, 3811–3819.
10. Schatz, P. N.; Mowery, R. L.; Krausz, E. R. *Mol. Phys.* **1978**, *35*, 1537–1557.
11. Solomon, E. I.; Pavel, E. G.; Loeb, K. E.; Campochiaro, C. *Coor. Chem. Rev.* **1995**, *144*, 369–460.
12. Kramers, H. A. Proceedings of the Section of Sciences, Koninflife Akad. Van Wetenschappen; Amsterdam, 1930; pp 962–965.
13. Abragam, A.; Bleaney, B. *Electron Paramagnetic Resonance of Transition Ions*; Dover Publications: New York, 1986.
14. Neese, F.; Solomon, E. I. *Inorg. Chem.* **1999**, *38*, 1847–1865.
15. Oganesyan, V. S.; George, S. J.; Cheesman, M. R.; Thomson, A. J. *J. Chem. Phys.* **1999**, *110*, 762–777.
16. Oganesyan, V. S.; Thomson, A. J. *J. Chem. Phys.* **2000**, *113*, 5003–5017.
17. Fujisawa, H.; Hayaishi, O. *J. Biol. Chem.* **1968**, *243*, 267–281.
18. Bull, C.; Ballou, D. P.; Otsuka, S. *J. Biol. Chem.* **1981**, *256*, 12681–12686.
19. Wasinger, E. C.; Davis, M. I.; Pau, M.; Orville, A. M.; Zaleski, J. M.; Hedman, B.; Lipscomb, J. D.; Hodgson, K. O.; Solomon, E. I. *Inorg. Chem.* (in press).
20. Orville, A. M.; Lipscomb, J. D. *J. Biol. Chem.* **1993**, *268*, 8596–8607.
21. Brown, C. A.; Pavlosky, M. A.; Westre, T. E.; Zhang, Y.; Hedman, B.; Hodgson, K. O.; Solomon, E. I. *J. Am. Chem. Soc.* **1995**, *117*, 715–732.
22. Solomon, E. I. *Inorg. Chem.* **2001**, *40*, 3656–3669.
23. Solomon, E. S.; Brunold, T. C.; Davis, M. I.; Kemsley, J. N.; Lee, S-.K.; Lehnert, N.; Neese, F.; Skulan, A. J.; Yang, Y-.S.; Zhou, J. *Chem. Rev.* **2000**, *100*, 235–349.

Comprehensive Coordination Chemistry II
ISBN (set): 0-08-0437486

Volume 2, (ISBN 0-08-0443249); pp 339–349